Evidence for vapor transport of the base and precious metals in the Panormos Bay Ag-Au-Te deposit, Tinos Island, Cyclades

Stylianos F. Tombros*, Michalis Fitros

Department of Geology, University of Patras, Rion, 26500 Patras, Greece

ARTICLE INFO

ABSTRACT

Tellurium-bearing, base and precious metal sulfides from the Au-Ag-Te mineralization at Panormos Bay, Tinos Island, Cyclades, preceded and followed the main telluride-forming event. Ore petrography and chemistry of the sulfides suggest that they have precipitated under supersaturation conditions, i.e., grown with hopper habit, enriched in Zn, Fe, Ag, Cd and Pb, and Te in stage II, III and VI sulfides and incorporate nanoparticles with variable Ag/(Pb + Ag + Cu + Fe + Zn)% values. The noble gas, i.e., He, Ar and Ne isotope compositions obtained from these sulfides form two distinct populations, the "Liquids" and "Vapors". All these features constitute overwhelming evidence that favors vapor transport for the base and precious metals by the vapor-like Panormos ore fluid.

The widespread occurrence of CO_2-effervescence and boiling at the Panormos Bay Au-Ag-Te ores provoked degassing of the CO_2, $HCl_{(g)}$, $H_2S_{(g)}$, $H_2Te_{(g)}$, $Te_{2(g)}$, light noble gas isotopes (^{3}He, ^{36}Ar, ^{20}Ne, and ^{21}Ne), base- and precious-bearing laden vapors from the mineralizing fluid and transported a fraction of the base and precious metals to vapor. Geochemical simulation suggests that supersaturation in the vapor phase, rapid up-vapor transport, and subsequent condensation in the Panormos Bay ore solution of $H_2Te_{(g)}$, $Te_{2(g)}$, and base and precious-bearing vapors led to the precipitation of sulfide (stages II, III and VI) and telluride (stage V) mineral assemblages.

1. Introduction

In the vast majority of the world-class Au-Ag-telluride deposits (e.g., Acupan, Philippines, Cooke and McPhail, 2001; Emperor, Fiji, Ahmad et al., 1987; Porgera, Papua New Guinea, Ronacher et al., 2004; Golden Sunlight, Montana, Spry et al., 1996, and Sandaowanzi, Great Hinggan Range, China, Zhai et al., 2018) the most efficient mechanism of deposition is precipitation of the base- and precious-tellurides from aqueous mineralizing liquids. The processes commonly involved include phase separation, mixing, simple cooling, and sulfidation or wall-rock interaction of the ore-forming fluids. The same appears to be true for the telluride-bearing, hydrothermal systems in Greece (e.g., Profitis Ilias-Chondro Vouno, Milos, Alfieris et al., 2013; Kassiteres-Sappes and Perama Hill, W. Thrace, Voudouris et al., 2006, 2011).

Furthermore precious metal transport by vapor phase is a process known since the early 1990's. Recent analyses of the trace-element composition of fumarolic gases and sublimates (e.g., Kilauea volcano, Hawaii Greenland and Aruscavage, 1986; Volcán Popocatépetl, Mexico, Larocque et al., 2008 and La Fossa volcano, Italy, Fulignati and Sbrana, 1998, see also Grundler et al., 2013), and vapor-rich fluid inclusions related to the widespread occurrence of phase separation (e.g., inclusions containing 180 ppm Te and ppm-levels of Au, Au-Te epithermal deposit, Rosia Montana, Romania, Wallier et al., 2006, and ≤670 ppm Te and ≤13 ppm Au, porphyry Cu-Mo-Au, Nevados de Famatina deposit, Argentina, Pudack et al., 2009), and experiments conducted on chloride-bearing ore-forming systems (e.g., Heinrich et al., 1992; Seward et al., 2014; Williams-Jones and Migdisov, 2014; Williams-Jones et al., 2002; Pokrovski et al., 2013; Grundler et al., 2013, and references therein) reveal that vapor transport of base and precious metals could play an important role as a mechanism of ore formation; a case that is currently underestimated. Seward et al. (2014), Williams-Jones and Migdisov (2014), Williams-Jones et al. (2002) and Pokrovski et al. (2013) have suggested that vapor is capable of dissolving and transporting orders of magnitude higher concentrations of Ag, Au, Zn and Cu in chloride-bearing water vapor, at the epithermal environment, than is predicted from equivalent volatility calculations. However, no direct petrographic and compositional evidence for vapor transportation is given for epithermal telluride deposits.

The epithermal Au-Ag-Te-bearing quartz veins at Panormos Bay, Tinos Island, Greece, display unusually high concentrations of base and

---

* Corresponding author.
  E-mail address: tombrosfs@gmail.com (S.F. Tombros).

precious metals in a variety of sulfides occurring in stages II, III and VI (of eight hypogene ore stages, details in Tombros et al. 2004, 2005, 2007 and 2010) which preceded and followed the main telluride-forming event (stage V). The current study is an extension of the work of Tombros et al. (2004, 2005, 2007, and 2010) which included mineralogical, compositional, textural, fluid inclusion, stable isotope data, along with thermodynamic modeling of the ore-forming fluids. The key conclusions of these studies were that phase separation i.e., CO_2-effervescence (related to stages II, III and IV) and boiling (linked to stages VI and VII) was associated with the formation of the Panormos telluride deposit, and primarily rapid up-vapor transport of the supersaturated tellurium-bearing vapors led them to condense as droplets, and resorbed into the ore fluid.

Ore petrography and chemistry of the Panormos Au-Ag-Te assemblage and thermodynamic calculations, in combination with our additional analytical data (e.g., new microprobe analyses and noble gas isotopic compositions of the sulfides of stages II, III and VI) were used to explain the observed enrichment of base and precious metals in the sulfides and tellurides (stage V). Based on these supplementary data, we explore herein the capacity of vapor to transport base and precious metals and the amplitude of such transport for the Panormos CO_2, $H_2Te_{(g)}$, $Te_{2(g)}$, base and precious laden fluid.

2. Geological setting of Tinos Island

Tinos Island is placed in the Attico-Cycladic Massif of Greece, which consists of a succession of three major Alpine nappes, overlying a Hercynian meta-igneous basement (Fig. 1, Okrusch and Bröcker, 1990; Jolivet et al., 2015): the lowermost Cycladic Basal unit (BU) represents a Late-Triassic to -Cretaceous platform of neritic meta-dolomites and -flysch (Xypolias et al., 2012). The BU is overlain by the Cyclades Blueschist unit (CBU) which comprises a Pre-Alpidic anatectic basement overlain by a volcano-sedimentary sequence (Fig. 1, Bröcker and Franz, 2005; Rabillard et al., 2015). The CBU has undergone two metamorphic events. The first of them, at 53–40 Ma, was at eclogite to blueschist facies conditions (Brichau et al., 2010), and it was followed by a retrograde greenschist to amphibolite facies overprint at ≥ 25 and ~12 Ma (Bolhar et al., 2010). The CBU is tectonically overlain by the Upper Cyclades unit (UCU) ofiolites (Fig. 1, Katzir et al., 2000).

The Tinos monzogranite-to-granodiorite intrudes at ~14 to 18 Ma all the above nappes, in the eastern part of the island (Fig. 1, Bröcker and Franz, 1998; Brichau et al., 2007) and has resulted in extensive contact metamorphism (Stolz et al., 1997). The contact aureole comprises an inner zone of pyroxene- and amphibole-hornfelses and pyroxene-garnet skarns that contain scheelite mineralization, and an outer zone of albite-epidote hornfelses (Fig. 1, St. Seymour et al., 2009). The granodiorite was intruded at its borders by a ~15–14 Ma boron- and fluorine-rich leucogranite (Fig. 1, Mastrakas and St. Seymour, 2000). The Tinos leucogranite is genetically related to both the formation of the scheelite skarn and Panormos Bay Au-Ag-Te mineralization (Fig. 1, Tombros et al., 2007, 2010; St. Seymour et al., 2009).

The Au-Ag-Te mineralization at Panormos Bay is hosted in a stockwork of quartz veins ~16 km west from the tectonic-intrusive contact of the Tinos leucogranite (Fig. 1, Tombros et al., 2007, 2010). The host rocks are the Triassic, thick-bedded, BU dolomitic marbles (Tombros et al., 2007, 2010). The mineralized epithermal vein system comprises a total of 30 nearly parallel, high-angle, syntaxial, quartz veins which occupy a conjugate system of NE- to NNE-trending,
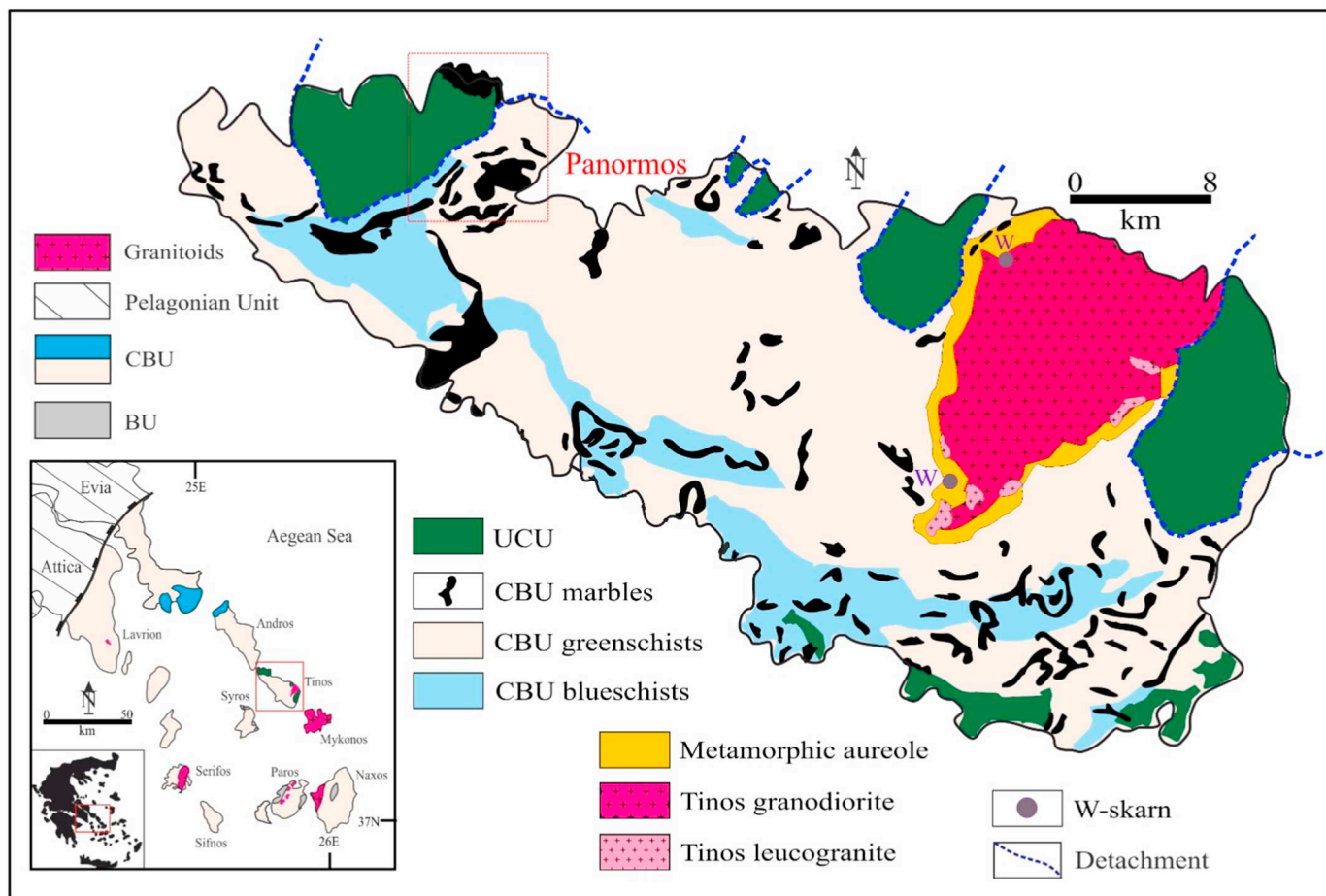

Fig. 1. Map showing generalized geology of Tinos Island, the location of W-scheelite skarn mineralization (W) and of the Panormos Bay Au-Ag-Te mineralization (modified after Melidonis, 1980; Mastrakas and St. Seymour, 2000; Tombros et al., 2007; Mehl et al., 2007).

sinistral and NW- to WNW-trending, dextral strike-slip faults. These veins form two generations of milky and clear veins (Tombros et al., 2007, 2010). The older milky quartz veins (≤ 2 m wide), trend NE to NNE which consist of pyrite, tetrahedrite, chalcopyrite and bornite ores. The younger clear quartz veins (≤ 0.5 m in width) trend NW to WNW, crosscut and replace the milky quartz veins, display open space filling textures and contain galena mineralization. Alteration zones that develop, in the BU marbles, around the milky quartz veins comprise tourmaline, calcite, talc, brucite, and Mg-enriched muscovite. Clear quartz veins are bordered by alteration envelopes containing chlorite, epidote, albite, and Ca-enriched muscovite (Tombros et al., 2007, 2010).

3. Analytical methods

Mineral compositions from stages II, III and VI of the Panormos Bay telluride mineralization (e.g., samples MT1 a, b and c, MT6 a and b, MT10 and MT20) were determined using a JEOL 8900 Superprobe equipped with wavelength, energy dispersive and back-scattered detectors and a xClent system for ppm-level resolution at the Microprobe Center of the Department of Earth and Planetary Sciences Department, at McGill University. Operating conditions were an acceleration voltage of 15 kV, a beam current of 10 nA, and a counting time of 20 s for all elements except 50 s for As and Te and 100 s for Ag. Digital scans and X-Ray mapping in WDS mode were also used to detect the distribution of the trace elements of the sulfides and tellurides. Standards used for ore minerals were natural chalcopyrite, tetrahedrite, tennantite, stibnite, pyrite, sphalerite, galena, synthetic CoNiAs, SnO_2 and CdTe, and the native metals Ag, Au and Se. The measured X-ray lines were Ag *La*, Sb *La*, Cu *Ka*, Fe *Ka*, Pb *Ka*, Au *Ma*, Mn *Ka*, Se *La*, Bi *La*, Cd *La*, Te *La*, and S *Ka*. ZAF corrections were made with proprietary JEOL software. A minimum of five analyses was obtained from each sample and three from each crystal.

Nineteen samples of sulfides that already have used for microprobe analyses, i.e., stage I pyrite, stage II tetrahedrite-tennantite and solid solution members, stage III chalcopyrite and bornite and stage VI galena were analyzed for their noble gas isotopic compositions. These were handpicked after examination under a binocular microscope to ensure textural equilibrium and a purity of better than 98%. Helium, argon, and neon isotope compositions were measured with a MI-1201IG inert gas mass spectrometer, at the Institute of Mineral Resources, Chinese Academy of Geological Sciences (CAGS). We have followed the analytical procedure of Wang et al. (2008) and Kendrick and Burnard (2013). The released noble gases were purified four times by titanium sponge (at 800 °C, for 20 min) and zircon-aluminum getters (at 450 °C, for 10 min) and active carbon cooling trap with liquid nitrogen (at −196 °C, for 40–60 min). This treatment was to remove the bulk of any possible active gases (e.g., H_2O and CO_2) and separate He from Ar and Ne. The released He, Ar and Ne were admitted to the spectrometer and then analyzed. The blank levels of ^{4}He and ^{3}He, ^{40}Ar and ^{36}Ar and ^{20}Ne and ^{22}Ne were 10^{-7}, 10^{-13} and 10^{-7} cm^3 STP/g. Results for He are reported as R/R_A ratios, where R is ^{3}He/^{4}He ratio of the sample and R_A is that of air, i.e., ^{3}He/^{4}He = $1.4 \cdot 10^{-6}$, ^{40}Ar/^{36}Ar = 295.5 and ^{21}Ne/^{22}Ne = 0.029.

4. Results

4.1. Petrography, mineralogy and ore chemistry of the Au-Ag-Te paragenesis

Over seventy ore and gangue minerals have been identified, at Panormos Bay ores (Tombros et al. 2004, 2005, 2007 and 2010). These occur in eight paragenetic stages of hypogene mineralization (I to VIII) and a later supergene stage (IX) (Table 1, details in Tombros et al. 2004, 2005, 2007 and 2010). The ore petrography, mineralogy and paragenetic sequence of these ores have been studied in detail by Tombros

et al. (2004, 2005, 2007 and 2010), and is briefly summarized herein focusing on stages II, III and VI (Fig. 2a, b, c and d) to provide a framework within which enable us to evaluate the base and precious metals contents of these Te-bearing sulfides.

4.1.1. Pre-Telluride stages

Stage I comprises milky quartz and pyrite (containing up to 0.02 apfu Au, cf. Table 3, Tombros et al., 2007, 2010) that is intimately intergrown with pyrrhotite and arsenopyrite. Stage II is dominated by fahlole minerals, i.e., tetrahedrite, tennantite, solid solution members and rare goldfieldite; with Sb/(Sb + As)% ratios ranging from 10 to 97. Ore petrography suggests that occasionally these minerals, and especially the tetrahedrite-tennantite solid solution crystals display distinctive hopper/skeletal habit depicting elevated rates during their growth (see also Andreassen and Lewis, 2017). This growth habit is assumed to be associated to elevated growth rates for certain parts of the crystal that leads to skeletal growth (Fig. 2a, also see Tombros et al., 2010, cf. Fig. 3; Andreassen and Lewis, 2017). Yudovskaya et al. (2006) reported the formation of such skeletal textures for magnetite, ferberite and pyrrhotite (cf. Fig. 6) from the Kudryavy volcano, Kurile Islands and attributed them to fast precipitation from a low-density gas phase under supersaturated conditions.

The fahlole minerals are replaced by stage III chalcopyrite and bornite. In some cases, chalcopyrite encrusts and replaces bornite which remains as unreplaced "islands" and vice versa (Fig. 2b). This texture, according to Saunders (2012), supports precipitation for stage III minerals in response to rapidly fluctuating conditions. The formation of hopper tetrahedrite-tennantite solid solution crystals and chalcopyrite-bornite "islands" may have been resulted from supersaturation of the ore-forming fluid, as a result of condensation of vapor. Under such conditions, Tempest and Ballentyne (1974) have experimentally grown synthetic greenockite and sphalerite. However, alternative interpretations for the formation of these skeletal crystals include decreasing growth rates, undercooling of the ore fluid, evaporation versus condensation, simple replacement processes and non-equilibrium conditions throughout their deposition (Andreassen and Lewis, 2017). Sulfosalts of Sn, As, Sb including stannite, boulangerite, bournonite, laggisite, luzonite, and arsenides of Ni and Co, i.e., niccolite and gersdorffite occur in stage IV (Table 1) as subhedral disseminations or granular and fibrous grains. These comprise up to 0.1 apfu Ag, Au, Sn and Zn, and up to 0.5 Cu (Tombros et al., 2007, 2010 cf. Table 3).

4.1.2. Telluride stage

Stage V consists of three sub-stages, i.e., early, middle, and late which contain Ag-, Cu-, and Au-bearing tellurides (Tombros et al., 2004, 2007, 2010). The main tellurides that occur in the early stage V are hessite and altaite (Table 1, Fig. 2c and d). These intergrowths with sylvanite and native Te, stützite and cuprian cervelleite (Table 1, details in Tombros et al., 2004, 2007, 2010). Melonite is the major telluride in middle stage V and intergrowths with rickardite, vulcanite and weissite (Table 2, details in Tombros et al., 2004, 2007, 2010). Late stage V comprises the assemblage kostovite (≤ 0.01 apfu Ag, Tombros et al., 2004, 2007), krennerite, petzite, calaverite (≤ 0.01 apfu Ag, Tombros et al., 2004, 2007) and unnamed Ag-Au-Cu sulfotellurides (Table 2, details in Tombros et al., 2004, 2007, 2010).

4.1.3. Post-Telluride stages

In stage VI, galena coexists with minor betekhtinite (≤ 0.02 apfu Ag) and argentite. These galena crystals in some cases contain arbitrarily distributed hessite and altaite which are also attributed to rapid up-vapor transport and subsequent condensation (Fig. 2c and d, see also Tombros et al., 2010). Stage VII is dominated by colloform sphalerite which is intergrown with greenockite, zincian-greenockite (containing ~0.35 apfu Zn, Tombros et al., 2005) and magnetite (Table 1). Lastly, stage VIII veins contain native gold (≤ 0.02 apfu Cu, Tombros et al., 2005), native silver (≤ 0.01 apfu Zn, Tombros et al., 2007), native
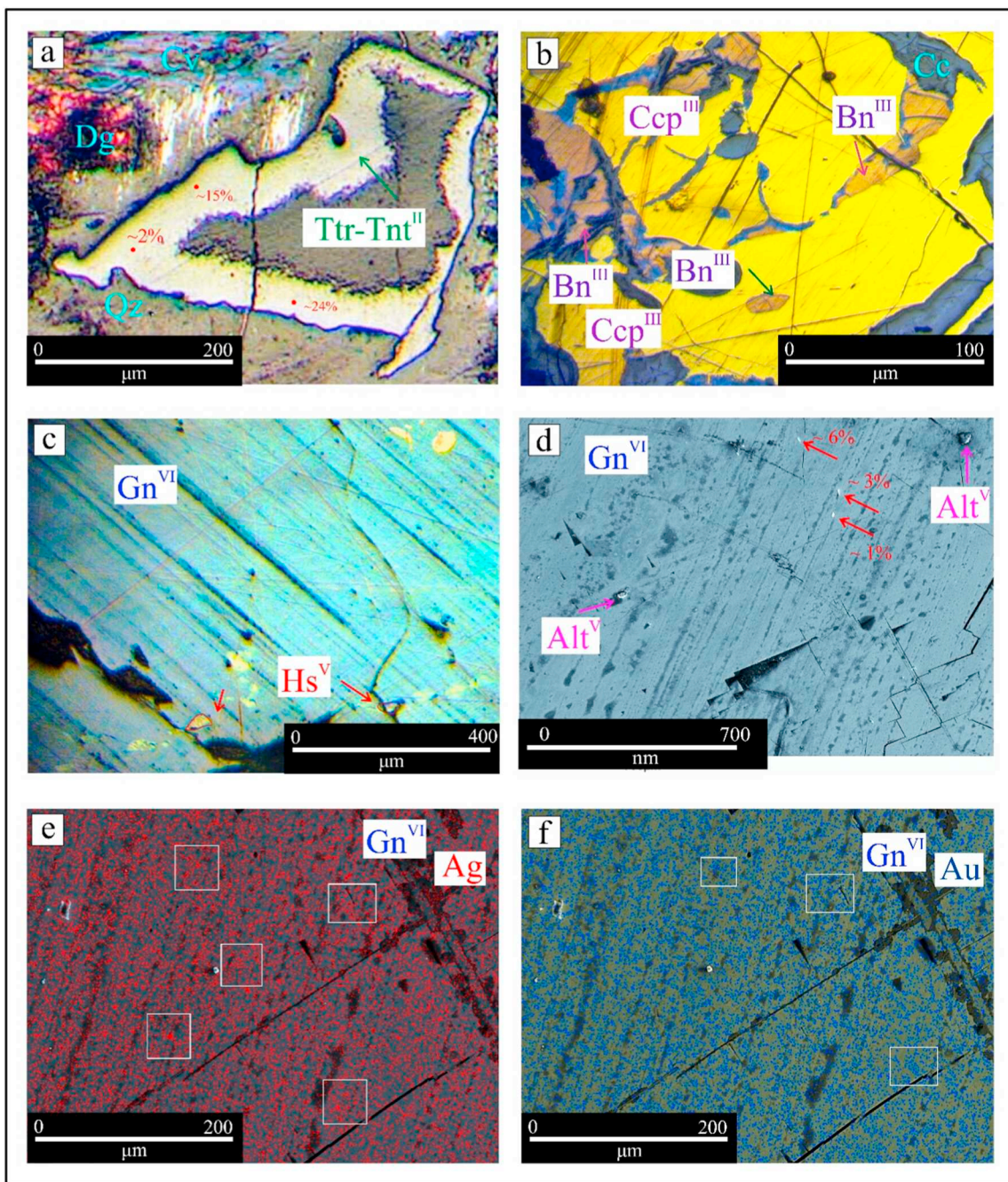
Table 1

Ore paragenesis and hypogene fill minerals from Panormos Bay Au-Ag-Te mineralization, Tinos.

Mineral stages	Stage I	Stage II	Stage III	Stage IV	Stage V	Stage VI	Stage VII	Stage VIII
Milky quartz	■■■■■■	■■■■■■	■■■■■■	■■■■■	■■			
Calcite		■■■■■■	■■■■■■	■■■■■	■■			
Clear quartz					■■	■■■■■■	■■■■■■	■■■■■■
Talc		■■■■■■	■■■■■■	■■■■■	■■			
Chlorite					■■	■■■■■■	■■■■■■	■■■■■■
Muscovite	■■	■■■■■	■■■■■	■■■■■	■■■■■	■■■■■	■■■■■	■■■■■
Albite	■■	■■■■	■■■■	■■■■	■■■■	■■■■	■■■■	■■■■
Epidote					■■	■■■■■■	■■■■■■	■■■■■
Brucite		■■■■	■■■■	■■■■	■■			
Pyrite	■■■							
Pyrrhotite	■■							
Arsenopyrite	■■							
Tetrahedrite		■■■■■■						
Tennantite		■■■■						
Goldfieldite		■■						
Chalcopyrite			■■■■■■					
Bornite			■■■■■■					
Mawsonite				■■■				
Stannite				■■■				
Boulangerite				■■				
Bournonite				■■				
Luzonite				■■				
Famatinite				■■				
Laggisite				■■				
Niccolite				■■				
Gersdorffite				■■				
Hessite[A]					■■■			
Stützite[A]					■■			
Altaite[A]					■■■			
					■■			
Sylvanite[A]					■■			
Cervelleite[A]					■			
Native Te[A]					■			
Melonite[B]					■■			
Rickardite[B]					■			
Vulcanite[B]					■			
Weissite[B]					■			
Calaverite[C]					■■			
Krennerite[C]					■			
Kostovite[C]					■■			
Petzite[C]					■■			
New Sulfotelluride[C]					■			
Galena						■■■■■■■■		
Argentite						■■		
Betekhtinite						■■		
Sphalerite							■■■■■	
Greenokite							■■■	
Magnetite							■■	
Native Au								■■■
Native Ag								■■■
Native Cu								■■
Native As								■■
Stromeyerite								■■
Pyrargyrite								■■

A = Early, B = Middle and C = Late telluride stage V.

copper (≤ 0.02 and 0.01 apfu Ag and Au, Tombros et al., 2004, 2007), native arsenic, stromeyerite and pyrargyrite (Table 1, Tombros et al., 2007, cf. Table 2).

4.2. Base and precious metals micro-contents of the sulfides and tellurides

Pokrovski et al. (2013) have suggested that new insights into the vapor transport of economic base and precious metals like Cu, Fe, Zn Au, and Ag in epithermal deposits can be obtained by using, amongst other methods, microprobe analysis of the metallic minerals. Under their perspective, we have analyzed the trace element contents of stages II, III and VI sulfides and stage V tellurides.

4.2.1. Pre-Telluride stages

The fahlole family minerals from stage II include zincian-argentian-cadmian-tellurian-tetrahedrite, zincian-ferric-cadmian-tellurian-tetra-hedrite-tennantite solid solutions, argentian-cadmian tennantite and argentian-goldfieldite $[Cu_6Cu_4Te_2(As,Sb)_4S_{13}]$ (Table 2, see also Tombros et al., 2007, 2010). Tetrahedrite crystals contain up to 9.9 wt % Cd and 1.3 wt% Ag, tennantite up to 4.7 wt% Zn, 2.0 wt% Fe and 1.5 wt% Cd, and goldfieldite up to 1.2 wt% Ag. Tennantite-tetrahedrite solid solutions comprise up to 7.3 wt% Zn, 3.5 wt% Ag, 1.9 wt% Cd and 0.6 wt% Fe. These values correspond up to 1.8 Zn, 1.5 Fe, 0.5 Cd, and 0.5 Ag in apfu (Table 2, Fig. 3a, b, and c). Their formulae, i.e., $(Cu_{9.9-10.6}Zn_{0-1.8}Fe_{0-1.5}Cd_{0-0.5}Ag_{0-0.5})_{\Sigma=12}(As_{0.7-3.6}Sb_{0.4-3.3})_{\Sigma=4}(-S_{11.1-13}Te_{0-1.9})_{\Sigma=13}$ suggest that for every 12 atoms in the M site there

Fig. 2. Representative photomicrographs of: (a). Tetrahedrite-tennantite (Ttr-Tnt^{II}) solid solution (Sb/(Sb + As)% ratios of 52), crystals intergrown with quartz (Qz) that have grown with hopper habit. These crystals contain up to 5.1 wt% Zn, 2.0 wt% Cd, 0.6 wt% Fe, 2.2 wt% Ag and 2.6 wt% Te and are characterized by variable Ag/(Pb + Ag + Cu + Fe + Zn)% ratios that range from ~2 to ~24. Supergene digenite (Dg), and covellite (Cv) are also shown (scale bar = 200 μm), (b). Chalcopyrite (Ccp^{III}, with 1.2 wt% Ag and 0.6 wt% Te) encrusts and replaces bornite (Bn^{III}, with 0.6 wt% Ag and 10.8 wt% Te) which remains as unreplaced "islands" and vice versa. The chalcopyrite and bornite crystals are coroneted by supergene chalcocite (Cc) (scale bar = 100 μm), (c). Galena (Gn^{VI}, with 0.4 wt% Cu, 0.2 wt% Ag and 2.0 wt% Te) that contains randomly distributed hessite (Hs^{V}, with 1.0 wt% Cu, 0.3 wt% Au) (scale bar = 400 μm), (d). Galena (Gn^{VI}, with 1.8 wt% Cu, 0.1 wt% Ag and 0.1 wt% Te) which contains altaite (Alt^{V}, with 1.0 wt% Cu, 0.2 wt% Ag and 0.6 wt% Au) (scale bar = 700 nm), and (e, f). X-ray map of Ag (La 1) and Au (Ma 1) of the same crystals revealing the spotty distribution for the precious metals. The analyzed galena crystals have incorporated nanoparticles that display variable Ag/(Pb + Ag + Cu + Fe + Zn)% values ranging from ~1 to ~6 (scale bar = 200 μm). Abbreviations: Ttr-Tnt^{II}: stage II tetrahedrite-tennantite solid solution, Dg: Digenite, Cv: Covellite, Qz: Quartz, Fe-Mg Ox: Fe-Mg Oxides, mainly goethite, Ccp^{III}: Stage IIII chalcopyrite, Bn^{III}: Stage III bornite, Cc: Chalcocite, Galena: Gn^{VI}: Galena, Hs^{V}: Stage V hessite (mineral abbreviations are after Whitney and Evans, 2010).

is a probable maximum substitution of 4 Zn, Cd, Fe, and Ag atoms. Furthermore plotting the fahlore mineral compositions on Sb/(Sb + As)% versus Fe/(Fe + Zn)% and Cd/(Cd + Zn + Fe)% diagrams (Fig. 3a, b, and c) provide evidence for Fe (e.g., Fe/(Fe + Zn)% ratios of ≤ 1.5 and ~5 to ~30) and Cd enrichment in these minerals (e.g.,Cd/(Cd + Zn + Fe)% ≤ 2 and ~5 to ~30, Table 2). Thus, on the Sb/

(Sb + As)% versus (Au + Ag)/(Au + Ag + Cu)% plot (Fig. 3c) as tennantite become richer in Sb the amount of Ag increases (e.g., (Au + Ag)/(Au + Ag + Cu)% ≤ 2 and 3 to 4, Table 2).

Stage III chalcopyrite (e.g., CuFe(S$_{1.8-2.0}$Te$_{0-0.2}$)$_{\Sigma=2}$) and bornite (e.g., Cu$_{4.8-5}$Ag$_{0-0.2}$)$_{\Sigma=5}$Fe(S$_{3-4}$Te$_{0-0.6}$)$_{\Sigma=4}$) comprise up to 4.2 wt% Ag, 1.2 wt% Pb and 0.3 wt% Zn which correspond up to 0.2 Ag and 0.1

Table 2
Electron microprobe analyses of, stage II-fahlole, stage III-chalcopyrite and bornite and stage VI-galena from Panormos Bay Au-Ag-Te mineralization.

Mineral	n = 18[1]	n = 10[2]	n = 1[3]	n = 1[4]	n = 10[5]	n = 13[6]	n = 19[7]
wt%							
Cu	37.03–40.91	43.77–45.83	44.84	39.05	55.45–63.58	34.02–34.83	0.00–1.81
Ag	0.42–2.33	1.42–1.87	0.31	1.24	0.33–4.22	0.05–0.11	0.00–0.22
Au	0.00–0.03	0.00	0.00	0.00	0.00	0.00	0.00
Fe	0.04–0.61	≤0.01	1.55	0.08	10.34–11.05	27.99–30.47	0.00–0.03
Pb	0.04–0.48	≤0.01	1.11	0.00	0.03–0.73	0.00–0.23	81.60–87.00
Cd	0.00–2.40	0.08–1.12	3.01	0.98	0.00	0.00	0.00
Zn	0.71–6.67	≤0.01	2.24	4.25	0.00–0.11	0.00–0.15	0.00–0.03
Te	0.02–2.61	18.12–19.38	1.56	0.12	0.00–9.10	0.00–8.72	0.00–4.37
As	3.07–10.03	2.23–3.78	19.63	2.08	0.00	0.00	0.00
Sb	10.89–25.45	6.38–7.10	0.00	25.01	0.00	0.00	0.00
Se	0.00–0.01	0.00	≤0.01	0.00	0.00	0.00	0.00–0.11
S	21.94–26.44	25.87–26.77	23.43	27.11	16.92–30.22	26.21–34.44	10.42–13.41
Total	99.31–99.90	99.41–99.94	99.22	99.93	99.44–100.03	97.34–99.97	97.78–99.99
Number of atoms based on (Calculations performed on apfu, and in per cent).							
Cu	10.19–10.46[c]	11.88–11.99[c]	10.47[c]	9.67[c]	4.72–4.96[e]	0.98–1.00[g]	0.00–0.07[g]
Ag	0.00–0.24[c]	0.01–0.14[c]	0.01[c]	0.17[c]	0.02–0.21[e]	≤0.01[g]	0.00–0.02[g]
Au	0.00	0.00	0.00	0.00	0.00	0.00	0.00
Fe	0.00–0.48[c]	0.00	0.44[c]	0.45[c]	1.00	1.00	≤0.01[g]
Pb	0.00–0.01[c]	0.00	0.15[c]	0.00	0.00–0.02[e]	0.00[g]	0.90–1.00[g]
Zn	1.29–1.57[c]	0.00	0.45[c]	1.17[c]	0.00–0.10[e]	≤0.01[g]	0.00
Cd	0.00–0.24[c]	0.14–1.44[c]	0.46[c]	0.55[c]	0.00	0.00	0.00
Te	0.00–0.65[d]	2.41–2.55[d]	0.10[d]	0.15[d]	0.00–0.49[f]	0.00–0.16[h]	0.00–0.11[i]
Sb	1.85–2.33[d]	0.79–0.91[d]	1.17[d]	3.11[d]	0.00–0.01[f]	0.00	0.00
As	0.77–2.15[d]	0.55–0.79[d]	2.73[d]	0.74[d]	0.00	0.00	0.00
Se	0.00	0.00	0.00	0.00	0.00	0.00	≤0.01
S	13.00	13.00	13.00	13.00	3.51–4.00[f]	1.84–2.00[h]	0.88–1.00
8	48–51	~41	10	97			
9	0.2–12.6	13.1–14.8	30.7	≤4.8			
10	0.2–12.2	0.00	4.8	33.6			
11	0.7–1.4	~1.6	0.8	≤4.4			
12					49–51	84–87	
13					0.0–1.5	0.1–0.3	
14					0.1–2.1	1–4.4	
15							93.1–99.9
16							0.0–6.6
17							0.0–2.1

Samples analyzed were MT1 a, b, and c, MT6 a, and b, MT10 and MT20.

[1, 2, 3, 4]Calculations were based on the proposed formulae by Trudu and Knittel (1998). For tetrahedrite-tennantite solid solutions[1] and tennantite[3] and tetrahedrite[4] end-members, as Te/Te + As + Sb ≤2 apfu, were based on 29 apfu, where: [c]Cu + Cb + Zn + Fe + Ag + Pb + Au = 13 and [b]Sb + As + Te = 4. For goldfieldite[2] as Te/Te + As + Sb ≥2 apfu, were based on the equation [29 − 4(Te/Te + As + Sb) − 0.5] apfu.

[5, 6]Calculations were based on the proposed formulae, for bornite[5] by Sugaki et al. (1975) and for chalcopyrite[6] (with fixed metal/sulfur ratio of 1). For bornite[5] where: [e]Cu + Ag + Pb + Ta = 5 and [f]S + Te + As = 4 and for chalcopyrite[6]: [g]Cu + Fe + Zn + Pb + Ag = 1 and [h]Sb + S + As + Te = 2. For galena[7]: [i]Sb + S + As + Te = 1.

For the fahlore family minerals: [8]Sb/(As + Sb)%, [9]Fe/(Fe + Zn + Cd)%, [10]Cd/(Fe + Zn + Cd)%, [11](Au + Ag)/(Au + Ag + Cu)%; for bornite and chalcopyrite: [12]Cu/(Cu + Fe)%, [13]Zn/(Cu + Fe)%, and [14]Ag/(Ag + Cu)%, and for galena: [15]Pb/(Pb + Ag + Cu + Fe + Zn)%, [16]Cu/(Pb + Ag + Cu + Fe + Zn)% and [17]Ag/(Pb + Ag + Cu + Fe + Zn)%.

Pb and Zn (all in apfu, Table 2, Fig. 3d and e). Their compositions cluster in two distinct populations marked by proportions of Zn/(Zn + Fe)% ≤ 0.5 and 0.8 to 1.5 and Ag/(Ag + Cu)% ≤ 0.5 and ≥2 to 4 (Fig. 3d and e, Table 2). Furthermore, higher Ag ± Au contents are compensated by a reduced number of Cu atoms (Fig. 3d and e). The magnitude of substitution in the M site for the fahlore minerals, coupled with their enrichment in Fe, Cd, and Ag (Fig. 3a, b, and c), as well as the elevated Zn and Ag contents incorporated in chalcopyrite and bornite (Fig. 3d and e) are attributed to supersaturation conditions related to a vapor phase enriched in base and precious metals.

4.2.2. Telluride stage

The (Cu + Ni + Pb)/(Au + Ag + Pb + Cu + Ni)% versus (Au + Ag)/(Au + Ag + Pb + Cu + Ni)% plot discriminates, on the basis of their base and precious metal content, the different telluride minerals (Fig. 3f). The analyzed tellurides are early stage V altaite (up to 3.1, 1.0 and 0.9 wt% Ag, Cu and Au, corresponding to ≤0.09 apfu Ag, Cu, and Au) and hessite (up to 1.5, 0.9 wt% Au and Cu or ≤0.04 apfu Au and Cu). These tellurides were replaced by middle stage V weissite (up to 0.3 wt% Ag or ≤0.07 apfu Ag), rickardite and melonite (with up to 3.9 and 0.3 wt% Au and Cu, corresponding to ≤0.06 apfu Au and Cu) and then by late-stage V calaverite (up to 0.3 wt% Ag or ≤0.03 apfu Ag), kostovite (up to 7.84 wt% Cu or ≤0.12 apfu Cu), krennerite, and petzite. Thus, from Fig. 3f, it is suggested that hessite and altaite are enriched up to ~7 in base (e.g., Cu, Ni, and Pb) and ~8% in precious metals (e.g., Au and Ag for altaite). Moreover, the Ag-bearing tellurides (e.g. hessite) deposit at higher (Cu + Ni + Pb)/(Ag + Cu + Pb + Ni + Au) values (Fig. 3f). Additionally, melonite and the Cu-tellurides, i.e., weissite, vulcanite and are enriched in (Ag + Au) up to ~5 and ~3.5% (Fig. 3f). The Cu-bearing tellurides (e.g., weissite and rickardite) precipitate at higher (Ag + Au)/(Ag + Cu + Pb + Ni + Au) values (Fig. 3f). Late Au- and Ag-bearing, i.e., calaverite, kostovite, krennerite and petzite contain Cu up to ~47% (Fig. 3f). From Fig. 3f, it is also implied that Cu and Au substitute for Ag in hessite, Cu, Au and Ag for Pb in altaite, Au and Cu for Ni in melonite and Cu for Au in kostovite. These substitutional solid solution relations could suggest that supersaturated conditions prevailed during precipitation of telluride stage V, for Cu and precious metals, and are attributed to vapor transport which increased their ionic content.
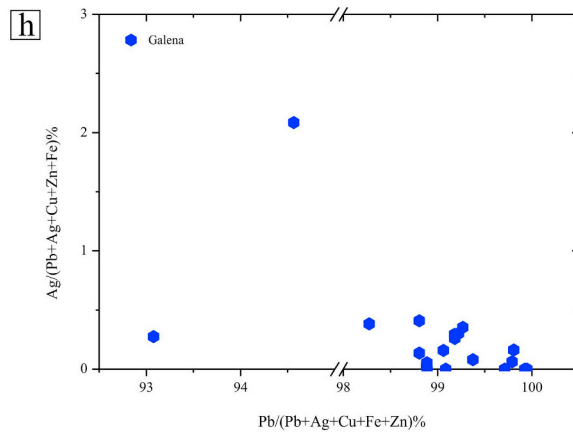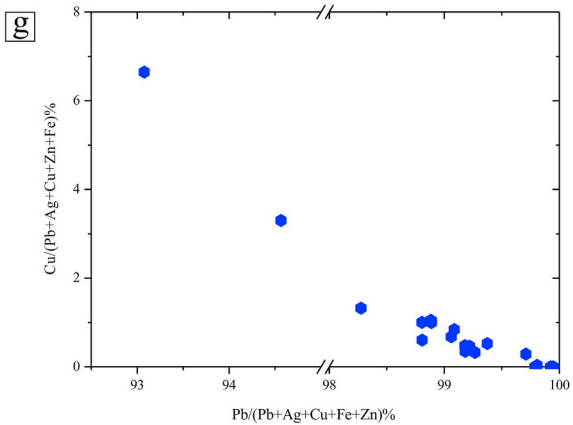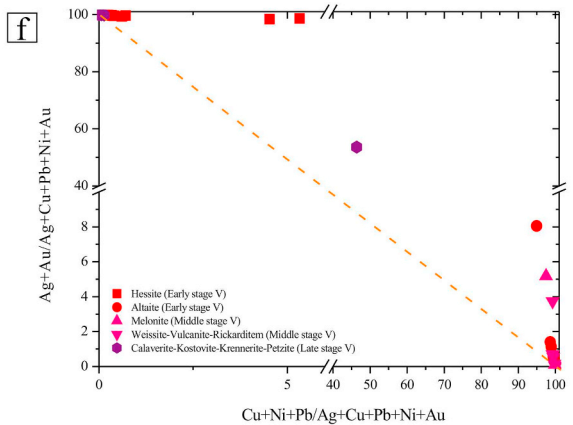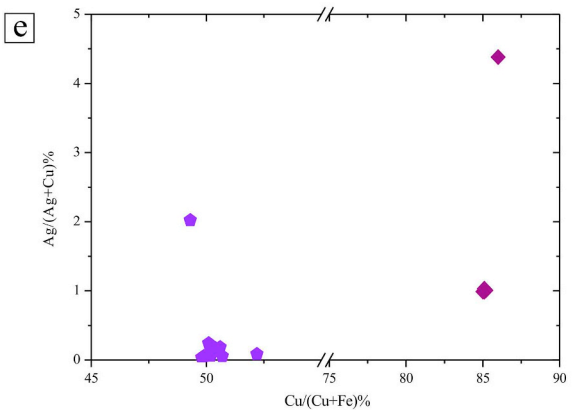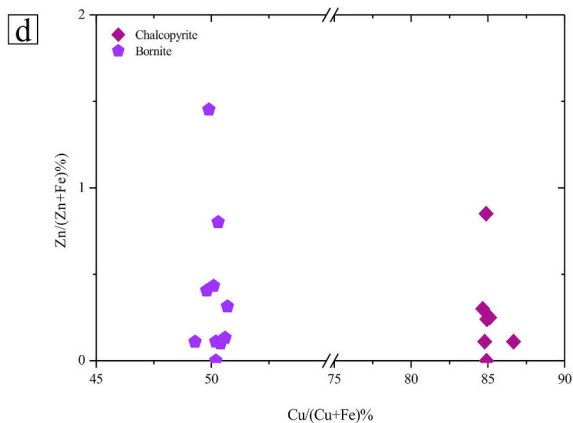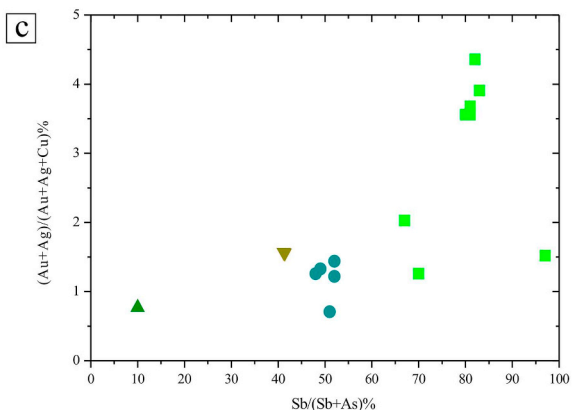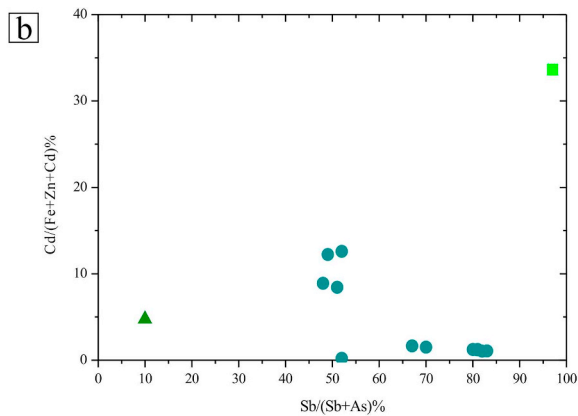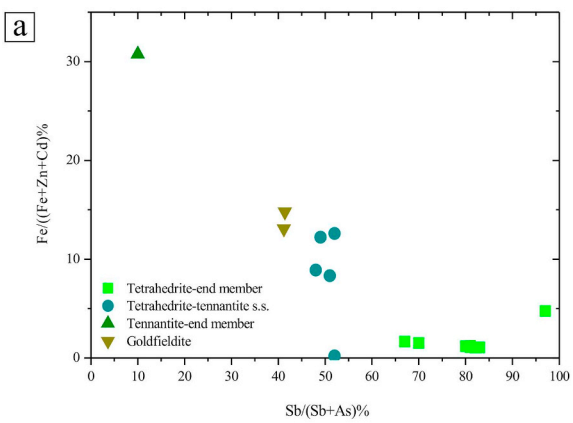
(caption on next page)

Fig. 3. Compositional diagrams of: (a): Sb/(Sb + As)% versus Fe/(Fe + Zn + Cd)%, (b): Cd/(Fe + Zn + Cd)%, and (c): (Au + Ag)/(Au + Ag + Cu)% for stage II fahlore family minerals, (d): Cu/(Cu + Fe)% versus Zn/(Zn + Fe)%, and (e) Ag/(Ag + Cu)% for stage III bornite and chalcopyrite, (f): (Cu + Ni + Pb)/(Au + Ag + Pb + Cu + Ni)% versus (Au + Ag)/(Au + Ag + Pb + Cu + Ni)% for the early, middle, and late-stage V tellurides, (g): Pb/(Pb + Ag + Cu + Fe + Zn)% versus Cu/(Pb + Ag + Cu + Fe + Zn)%, and (h): Ag/(Pb + Ag + Cu + Fe + Zn)% for stage VI galena at Panormos Bay Au-Ag-Te mineralization.

4.2.3. Post-Telluride stage

Stage VI galena (e.g., $(Pb_{0.9-1}Cu_{0.-0.1}Ag_{0-0.1})_{\Sigma=1}(S_{0.9-1}Te_{0.1})_{\Sigma=1}$) contains up to 1.0 wt% Ag and 0.9 wt% Cu, corresponding up to 0.1 apfu of Cu and Ag. Occasionally the analyzed galena crystals that enclose tellurides, i.e., hessite or altaite or both of them, have also incorporated nanoparticles ($\sim 10^{-7}$ to 10^{-8} m in size, Saunders, 2012) that display variable Ag/(Pb + Ag + Cu + Fe + Zn)% values ranging from ~1 to ~6 (Fig. 2d). Herein we should emphasize that due to the nanoscale dimensions of the analyzed particles, secondary emission effects from the enclosing galena are possible. The presence of such nanoparticles accommodated in the analyzed galena crystals is established by X-ray element maps for Ag and Au (Fig. 2e and f). The precious metals are organized following a spotty scattering mode in galena crystals, where Ag appears to be more enriched with respect to Au. Thus, in some spots of the X-ray mapped galena crystals the distribution of Ag and Au is more frequent and in others less (Fig. 2e and f). Galena compositions when plotted on the Pb/(Pb + Ag + Cu + Fe + Zn)% versus Cu/(Pb + Ag + Cu + Fe + Zn)% and Ag/(Pb + Ag + Cu + Fe + Zn)% diagrams, as the Pb/(Pb + Ag + Cu + Fe + Zn)% ratios increase (Fig. 2g and h), display an enrichment for Cu (e.g., Cu/(Pb + Ag + Cu + Fe + Zn)% ≤ 1 and 1.5 to ~6) and Ag (e.g., Ag/(Pb + Ag + Cu + Fe + Zn)% ≤ 0.5 and ≈2). The presence of nanoparticles in galena, as well as the observed scatter style on Fig. 3g and h, is also ascribed to supersaturation, due to vapor transport of the precious and base metals (Ag ± Au, Cu) at stage VI (also proposed for tellurium by Tombros et al., 2010). Yudovskaya et al. (2006) reported that the presence of condensates that contain plate-, sphere-, and icicle-like nanoparticles of native Se, Mo, Ag and Cu-Ni alloys from the Kudryavy volcano, Kurile Islands also suggest vapor transport and subsequent condensation. The sulfides from these condensates also enriched in some base and precious metals. For example, pyrite contains up to 70 ppm Ag and 13 ppm Zn, sphalerite ~330 ppm Ag and ~92 ppm Cd, magnetite ~33 ppm Cd and pyrrhotite 1.9 to 3.01 wt% Cu.

4.3. Noble gas isotopic compositions of the sulfides

He, Ar and Ne isotope compositions were obtained from fluids extracted from crystals of pyrite (stage I), tetrahedrite, tennantite and solid solutions (stage II), chalcopyrite and bornite (stage III) and galena (stage VI). The $^3He/^4He$ and $^{40}Ar/^{36}Ar$ compositions of these sulfides range from 0.009 to 0.098 and 324 to 1225 (Table 3, Fig. 4a). All these values recommend a crustal reservoir for the Panormos Bay ore fluids (see also Kendrick et al., 2001; Zhu et al., 2013). They additionally display $^{40}Ar/^4He$ and $^3He/^{36}Ar$ values ranging from 0.28 to 3.30 and 0.12 to 1.18 (Table 3, Fig. 4a).

From the $^3He/^4He$ and $^{40}Ar/^{36}Ar$ plot (Fig. 4a) it is evident that the analyzed sulfides display a distinct grouping in two populations, i.e., a group of low $^3He/^4He$ and high $^{40}Ar/^{36}Ar$ values (e.g., $^3He/^4He$ ≤ 0.03 and $^{40}Ar/^{36}Ar$ ≥ 900) and another set of high $^3He/^4He$ and low $^{40}Ar/^{36}Ar$ values (e.g., $3He/^4He$ ≥ 0.07 and $^{40}Ar/^{36}Ar$ ≤ 400). Moreover, the same sulfides were analyzed for their $^{20}Ne/^{22}Ne$ and $^{21}Ne/^{22}Ne$ compositions (Table 3, Fig. 4b). Their $^{20}Ne/^{22}Ne$ and $^{21}Ne/^{22}Ne$ ratios range from 9.86 to 12.25 and 0.0408 to 0.0599. From the $^{21}Ne/^{22}Ne$ versus $^{20}Ne/^{22}Ne$ plot (Fig. 4b), it is apparent that the ore fluids related to the Panormos Bay mineralization are also plotted in the "crust" field and display the same mode of grouping with Fig. 4a.

4.4. Initial composition of the Panormos ore fluid and physicochemical conditions of pre-, post- and telluride formation

We briefly summarize herein the physicochemical conditions prevailed during the deposition of the Panormos Bay Au-Ag-Te ores, estimated by Tombros et al. (2004, 2005, 2007 and 2010). Trapping temperatures and pressures range between ~200° and ~320 °C and ≤500 bars at salinities of 0.6 to 13.3 wt% NaCl equivalent. The Panormos mineralizing fluid is considered as a CO_2-rich bicarbonate ore-forming liquid (Tombros et al., 2010). It was suggested that has precipitated the Au-Ag-Te mineralization in response of CO_2-effervescence for the early mineralizing stages, i.e., stages II, III and IV, and boiling for stages VI and VII in the hydrothermal system. Phase separation occurred with maxima at temperatures of ~320°, ~290°, ~280°, ~260°, ~230°, ~220°, and ~210 °C (Tombros et al., 2007, 2010). Other calculated physicochemical parameters include pH = 4.6 to 6.5, $\log f_{S2} = -15$ to -10.9, $\log f_{O2} = -41$ to -31.5, $\log f_{Te2} = -10.7$ to -7.7, $\log f_{CO2} = -0.8$ to -0.2 and $\log f_{H2S} = -1.8$ to -1.7 (Tombros et al., 2007, 2010).

Chemical conditions of the base and precious metal sulfides were estimated from phase stability relationships of the coexisting Cu, Pb, and Ag chloride and mono- and bi-sulfide complexes. Temperatures of 270° and 220 °C representing the pre- (stage III, precipitation of chalcopyrite and bornite) and post-telluride stages (stage VI precipitation of galena) of Panormos Bay mineralization, and a pressure of 500 bars of vapor-saturated liquid is used. Calculations were accomplished only for these stages as the currently available experimental data for vapor speciation includes precious metals, and for the base metals only Cu and Zn (Seward et al., 2014; Williams-Jones and Migdisov, 2014; Williams-Jones et al., 2002; Pokrovski et al., 2013, and references therein).

Geochemical simulation utilizing the PHRQPITZ software (Plummer et al., 1988), was based on the calculated physicochemical parameters obtained from Tombros et al. (2007, 2010) for the calculation of the activity of chloride complexes over pH of the ore solution. This software incorporates the Pitzer specific-ion-interaction equations of state (Pitzer, 1979, 1986) using the properties of Plummer et al. (1988). All phases were considered to be ideal and individual ion activity coefficients of dissolved and gaseous species were obtained from Henley et al. (1984), Ahmad et al. (1987) and Tombros et al. (2010).

The initial composition of the Panormos Bay ore fluid, based on the results of the PHRQPITZ simulation, were $\log a_{\Sigma Cl^-(aq)} = -1.1$, $\log a_{HCl(aq)} = -5.4$, $\log a_{NaCl(aq)} = -1.4$, $\log a_{H2(aq)} = -7.8$, $\log a_{\Sigma H2Te(aq)} = -3.6$ (at T = 300 °C, pH = 4.6, Eh = 0.047 V, I = 0.4, $a_{H2O} = 0.995$, solvent mass = 1 kg, solution m = 1.01 kg, chlorinity of 0.2 m and d = 0.76 g/cm³, Tombros et al., 2007). The gaseous content of the vapor phase related to the deposition of tellurides of Panormos Bay mineralizing fluid was $\log f_{\Sigma H2Te(g)} = -4$, $\log f_{H2O} = -1.7$, $\log f_{H2(g)} = -7.8$, $\log f_{CO2} = -0.2$, $\log f_{Cl2(g)} = -10.4$, and $\log f_{O2(g)} = -35$, at 300 °C. We have also used the equations of Knight and Bodnar (1989) to estimate the critical P-T-d properties of the Panormos Bay ore fluid during phase separation. The critical T, P and d of this ore fluid were $T_{critical} = 412°$ and 402 °C, $P_{critical} = 317$ and 289 bars and $d_{critical} = 0.40$ and 0.53 cm³/g, for milky and clear quartz respectively, and for an average salinity of 4 and 3 wt% equivalent NaCl (Tombros et al., 2007). These critical conditions that Panormos Bay ore fluid was a highly mobile, vapor-like ore fluid (see also Pokrovski et al., 2013, cf. Fig. 1).

Table 3

He, Ar and Ne isotopic compositions of fluid inclusions in tetrahedrite, chalcopyrite, bornite, galena and pyrite Au-Ag-Te Panormos mineralization, Tinos.
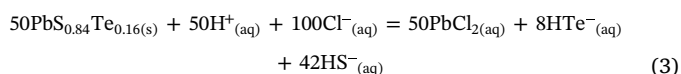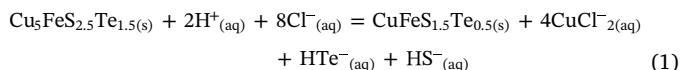
Minerals	$^4He^A$	$^3He^B$	$^3He/^4He^{C,1}$	$R/R_A{}^G$	$^{36}Ar^D$	$^{40}Ar^A$	$^{40}Ar/^{36}Ar^{E,2}$	$^{40}Ar/^4He$	$^3He/^{36}Ar^F$	$^4He/^{36}Ar^E$	$^{20}Ne^B$	$^{21}Ne^B$	$^{22}Ne^B$	$^{20}Ne/^{22}Ne$	$^{21}Ne/^{22}Ne$
Trt-Tnt	1789.7	135.5	0.076	0.05	153.1	4487.9	341.1	2.51	0.89	11.69	10.94	25.02	1.02	10.73	0.041
Trt-Tnt	1852.5	137.9	0.074	0.05	140.4	3638.7	385.8	1.96	0.98	13.19	15.30	21.04	1.26	12.14	0.059
Trt-Tnt	1782.2	126.1	0.071	0.05	136.2	3836.9	355.0	2.15	0.93	13.08	16.20	22.89	1.33	12.18	0.058
Trt-Tnt	2342.4	26.9	0.012	0.01	135.9	1237.5	1098.5	0.53	0.20	17.23	16.70	23.08	1.37	12.19	0.059
Trt-Tnt	2451.9	26.1	0.011	0.01	134.6	1235.9	1089.1	0.50	0.19	18.21	17.40	24.06	1.43	12.17	0.059
Trt-Tnt	767.3	19.2	0.025	0.02	167.1	1845.4	905.6	2.40	0.12	4.59	15.25	29.06	1.39	10.97	0.048
Trt-Tnt	1804.1	117.8	0.065	0.05	99.9	2008.3	497.3	1.11	1.18	18.06	18.01	30.06	1.55	11.62	0.052
Ccp	1463.4	137.5	0.094	0.07	188.8	4832.7	390.7	3.30	0.73	7.75	18.15	25.78	1.49	12.18	0.058
Ccp	1582.3	145.2	0.092	0.07	199.8	4935.1	404.9	3.12	0.73	7.92	15.50	21.84	1.27	12.20	0.058
Ccp	3546.1	34.7	0.010	0.07	126.7	1034.2	1225.4	0.29	0.27	27.98	16.05	22.94	1.31	12.25	0.057
Bn	3782.0	32.2	0.009	0.01	129.4	1058.0	1223.0	0.28	0.25	29.23	17.34	24.67	1.43	12.13	0.058
Bn	1752.0	158.8	0.091	0.07	175.7	4436.7	396.0	2.53	0.90	9.97	13.65	24.13	1.23	11.10	0.051
Gn	1592.2	123.6	0.078	0.06	130.1	3936.5	330.6	2.47	0.95	12.24	17.56	29.74	1.57	11.18	0.053
Gn	1479.1	122.4	0.083	0.06	127.5	3941.2	323.5	2.66	0.96	11.60	10.38	23.86	1.02	10.18	0.043
Gn	1399.3	121.2	0.087	0.06	134.7	4041.1	333.3	2.89	0.90	10.39	18.45	31.89	1.64	11.25	0.051
Gn	1433.8	32.3	0.023	0.02	168.1	1504.4	1117.0	1.05	0.19	8.53	11.89	26.67	1.14	10.43	0.043
Gn	1504.1	31.3	0.021	0.01	170.2	1493.1	1139.9	0.99	0.18	8.84	10.75	25.15	1.09	9.86	0.043
Py	1211.6	49.9	0.041	0.03	190.6	2235.734	852.3	1.85	0.26	6.36	16.20	29.06	1.46	11.09	0.050
Py	1208.5	51.1	0.042	0.03	200.0	2333.124	857.3	1.93	0.26	6.04	18.89	30.06	1.64	11.52	0.055

$^A10^{-7}$ and $^B10^{-13}$ cm³ STP/g, $^C10^{-6}$, $^D10^{-10}$ cm³ STP/g, $^E10^{-3}$, $^F10^{-4}$, ^GR_A represents the $^3He/^4He$ ratio in atmosphere, which is $1.4 \cdot 10^{-6}$.
[1] Mean of 0.054 and standard deviation of 0.034, [2] mean of 698 and standard deviation of 365, [3] mean of 1.82 and standard deviation of 0.99, [4] mean of 0.58 and standard deviation of 0.37, [5] mean of 77.2 and standard deviation of 41.1, [6] mean of 11.44 and standard deviation of 0.77, [7] mean of 0.53 and standard deviation of 0.06.
Trt-Tnt: Tetrahedrite-tennantite, Ccp: Chalcopyrite, Bn: Bornite, Gn: Galena, Py: Pyrite (Mineral abbreviations are after Whitney and Evans, 2010).

Simulation for stage III deposition was based on the equilibriums (1, 2) that involve the co-formation of the Te-rich bornite and chalcopyrite (~1.5 and ~0.5 apfu Te, Tombros et al., 2010). For the conditions of stage III (n = 1, Williams-Jones and Migdisov, 2014; Williams-Jones et al., 2002; Pokrovski et al., 2013, T = 270 °C, $loga_{HS^-(aq)}$ = −3.3, $loga_{HTe^-(aq)}$ = −4.3, $logfO_2$ = −33, $loga_{CuCl2(aq)}$ = −6.4 and pH = 5.4, details in Tombros et al., 2010, cf. Table 3) the Panormos ore fluid is considered as a $AgCl_{(g)}$- and $Te_{2(g)}$-bearing (see Grundler et al., 2013, cf. Fig. 12d, where the dominant species in the vapor phase is expected to be $Te_{2(g)}$) vapor-like fluid that condensed in the $CuCl_2^-$-bearing mineralizing liquid. Our results show that for equilibrium (1) and pH of 5.4, the $loga_{Cl^-}$ values are −1 and plot in the stability field of both $CuCl_2^-$ and $Cu(HS)_{(aq)}$ (Fig. 5a). For the vapor-dominated reaction (2) the $loga_{Cl^-}$ values range from −1 to −0.45 and these values plot in the stability field of both $AgCl_2^-$ and $Ag_{(aq)}$ (Fig. 5b).

$$Cu_5FeS_{2.5}Te_{1.5(s)} + 2H^+{}_{(aq)} + 8Cl^-{}_{(aq)} = CuFeS_{1.5}Te_{0.5(s)} + 4CuCl^-{}_{2(aq)}$$
$$+ HTe^-{}_{(aq)} + HS^-{}_{(aq)} \qquad (1)$$

$$AgCl_{(aq)} + H_2O_{(l)} = AgCl \cdot H_2O_{(g)} \qquad (2)$$

$$50PbS_{0.84}Te_{0.16(s)} + 50H^+{}_{(aq)} + 100Cl^-{}_{(aq)} = 50PbCl_{2(aq)} + 8HTe^-{}_{(aq)}$$
$$+ 42HS^-{}_{(aq)} \qquad (3)$$

Stage VI is simulated by utilizing the equilibriums (2) and (3) and the conditions reported by Tombros et al. (2010), cf. Table 3, i.e., T = 220 °C, $loga_{HS^-(aq)}$ = −4.5, $loga_{HTe^-(aq)}$ = −5.9, $logPbCl_{2(aq)}$ = −4.5 and pH = 6.1 which relate to the formation of the Te-rich galena (up to 0.16 apfu Te). We have also assumed that the same type of mineralizing fluid has condensed in the $Pb(HS)_{2(aq)}$-bearing ore liquid. Our results suggest that for equilibrium (3), and pH of 6.1 the $loga_{Cl^-}$ values increased (e.g., −0.15) and plot in the stability field of both $PbCl_{2(aq)}$ and $Pb(HS)_{2(aq)}$ (Fig. 5c). Under these conditions the dominant species in the vapor phase is expected to be $H_2Te_{2(g)}$ (see Grundler et al., 2013, cf. Fig. 12d). Nonetheless, for reaction (2) the $loga_{Cl^-}$ values are similar with the ones of stage III, i.e., range from −0.9 to −0.5 and plot in the same stability field (e.g., $AgCl_2^-$ and $Ag_{(aq)}$, Fig. 5d). Based on the phase stability relationships we note that there is a competition between the Cu and Ag chloride, mono- and bi-sulfide complexes which are transported at the vapor and/or the liquid

phase under supersaturation conditions; wherefrom $Cu(HS)_{(aq)}$ is expected to be more volatile than $CuCl_2^-$ (Archibald et al., 2002), and $AgCl_2^-$ than $Ag_{(aq)}$ (Migdisov et al., 1999). Such a competition mechanism could also be an important driver for precipitation as it affects the distribution of base and precious complexes of the liquid and gaseous phase or between them in the ore fluid (Rickard and Luther, 2006).

5. Discussion

He, Ar and Ne isotope compositions of stage I pyrite on the $^3He/^4He$ versus $^{40}Ar/^{36}Ar$ and $^{21}Ne/^{22}Ne$ versus $^{20}Ne/^{22}Ne$ plots (Fig. 4a and b) lay in the intermediate part of these plots and between the two formed populations that represent stages II, III and VI. As already discussed, the Panormos Bay Au-Ag-Te mineralization has precipitated in response of phase separation (Tombros et al., 2007, 2010). During phase separation steam escapes from the ore liquid and the dissolved gases move preferentially into the vapor phase.

The first CO_2-effervescence episode occurred at ~290 °C and resulted in the precipitation of stage II fahlore minerals. This effervescence event caused on the $^3He/^4He$ versus $^{40}Ar/^{36}Ar$ and $^{20}Ne/^{22}Ne$ versus $^{21}Ne/^{22}Ne$ plots (Fig. 4a and b), due to rapid transport of vapor, the formation of the two distinct populations for the fahlore minerals. As CO_2-effervescence proceeds the light ^3He, ^{36}Ar, ^{20}Ne, and ^{21}Ne isotopes preferentially fractionate in the gaseous phase of the Panormos ore fluid. Escape of the light noble gas isotopes (e.g., ^3He, ^{36}Ar, ^{20}Ne and ^{21}Ne) provoked a decrease of the $^3He/^4He$, $^{20}Ne/^{22}Ne$ and $^{21}Ne/^{22}Ne$ isotope compositions in the remaining ore liquid phase of the Panormos mineralizing fluid coupled with an increase of its $^{40}Ar/^{36}Ar$ compositions. Under such conditions, these isotopic ratios tend to concentrate in the left-top (Fig. 4a) and left-bottom side (Fig. 4b) of these plots (as recorded in the analyzed stage II fahlore minerals) which represent the "Liquids" population (labeled as L). Furthermore degassing of the light isotopes (e.g., ^3He, ^{36}Ar, ^{20}Ne and ^{21}Ne) led them to concentrate in the vapor phase. As result the $^3He/^4He$, $^{20}Ne/^{22}Ne$ and $^{21}Ne/^{22}Ne$ isotope compositions of the vapor of the Panormos mineralizing fluid tend to increase and $^{40}Ar/^{36}Ar$ compositions to decrease. These higher isotopic values represent the "Vapors" population (labeled as V).

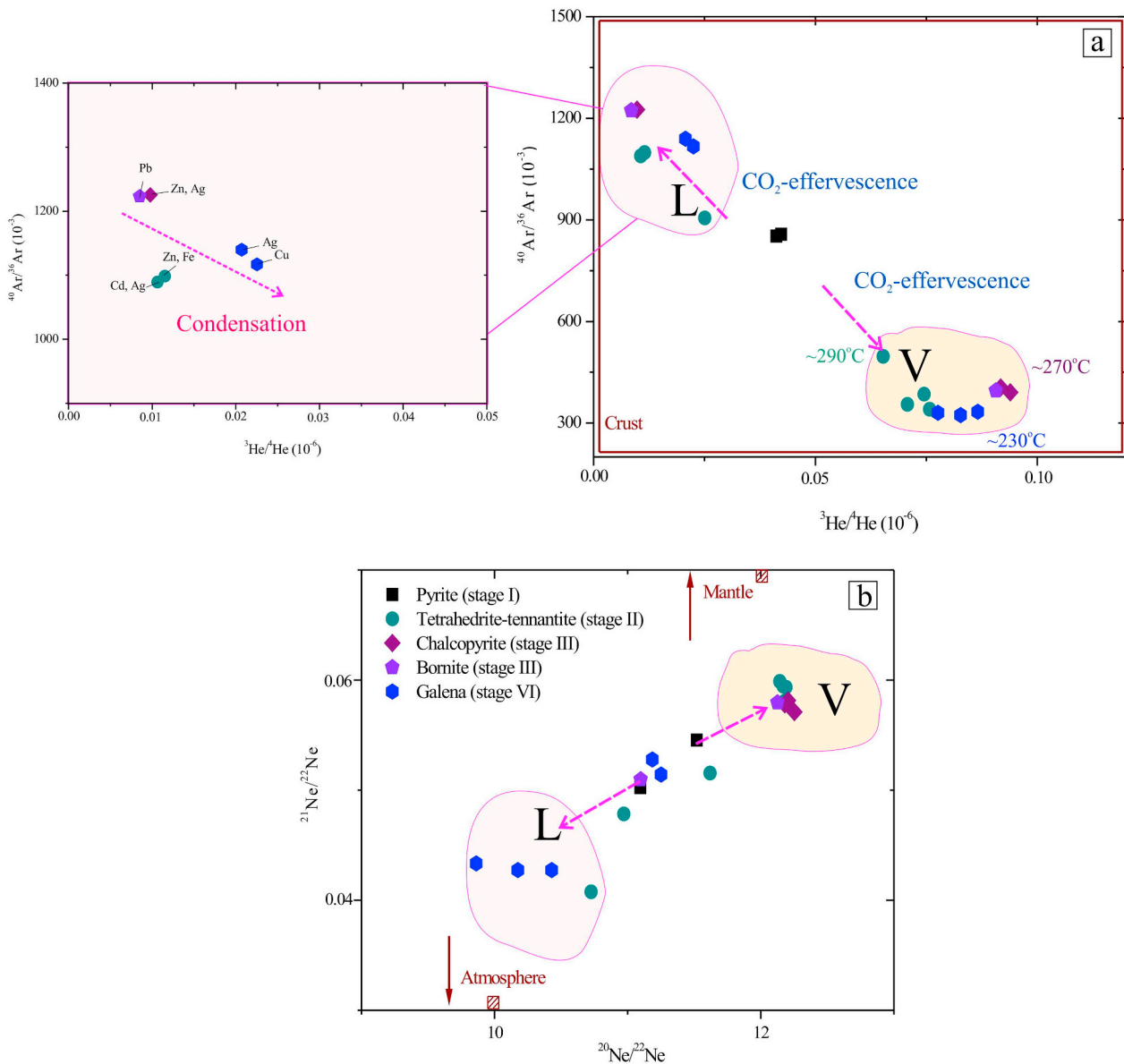Such a data grouping (Fig. 4a and b) probably constitutes the most

Fig. 4. (a): ^{3}He/^{4}He versus ^{40}Ar/^{36}Ar isotopic compositions from fluids extracted from crystals of pyrite (stage I), tetrahedrite, tennantite and solid solutions (stage II), chalcopyrite and bornite (stage III) and galena (stage VI) that display the effect of CO_2-effervescence. The data are grouped in two populations, where L represents the "Liquids" and V the "Vapors". Temperatures are obtained from (Tombros et al., 2007, 2010). The plot on the left is a detail of (a) and shows the effect of condensation in ^{3}He/^{4}He versus ^{40}Ar/^{36}Ar isotopic compositions of the analyzed sulfides. In each of these sulfides the type of base and precious metal which are enriched is also illustrated (as detected from microprobe analyses), i.e., Zn, Fe, Cd and Ag for tetrahedrite-tennantite (stage II), Pb for chalcopyrite and Zn, Ag for bornite (stage III), and Cu and Ag for galena (stage VI), and (b): ^{20}Ne/^{22}Ne versus ^{21}Ne/^{22}Ne isotopic compositions of the same sulfides. The "crust", "mantle", and "atmosphere" fields are from Zhu et al. (2013).

substantiated evidence that favors vapor transport of base and precious metals by the Panormos Bay vapor-like ore fluid. Alternatively, a part of the data may imply that there was an addition of meteoric waters that mixed with and diluted the Panormos ore fluid and lower both its ^{3}He/^{4}He and ^{40}Ar/^{36}Ar contents (see Tombros et al., 2007). The Panormos base and precious laden vapors have formed as the volatiles fractionate preferably in the vapor phase due to the CO_2-effervescence episode at ~290 °C. CO_2-effervescence tends to increase the magnitude of steam and other gases, i.e., CO_2, $HCl_{(g)}$, $H_2S_{(g)}$, $H_2Te_{(g)}$, $Te_{2(g)}$ as well as the light noble gas isotopes (e.g., ^{3}He, ^{36}Ar, ^{20}Ne and ^{21}Ne) that escape to vapor and raise vapor pressure (Williams-Jones and Migdisov, 2014; Williams-Jones et al., 2002; Pokrovski et al., 2013, and references therein). An increase of the vapor pressure of the Panormos ore fluid due to CO_2-effervescence and boiling (Tombros et al., 2010) most probably enhanced the formation of hydrated gas-base and precious

metal-complexes (e.g., as $CuCl \cdot nH_2O$ and $AgCl \cdot nH_2O$, at P ≤ ~200 bar, Williams-Jones and Migdisov, 2014; Williams-Jones et al., 2002; Pokrovski et al., 2013, and references therein). Additionally, elevated vapor pressure facilitated the transport and redistribution of the base and precious metals in the vapor as monochloride Cu and Ag gas-hydrated complexes (Seward et al., 2014; Williams-Jones and Migdisov, 2014). Metal-ligand complexation of these gas-hydrated complexes occurs either as vapor bubbles enclosed in the ore liquid or in the vapor or in the transitional zone between the vapor and liquid. The gas-hydrated complexes form more or less well-defined spheres around the metal cations that are surrounded by water molecules (Seward et al., 2014 cf. Fig. 1; Ohtaki and Radnai, 1993; Seward and Driesner, 2004). Simultaneously the loss of Cu, Ag (and Zn, Fe, and Cd, Fig. 4a) from the ore solution probably reflects a decrease in the $loga_{CuCl2^-}$ and $loga_{Cu(HS)(aq)}$ values of the fluid (Simon et al., 2006).

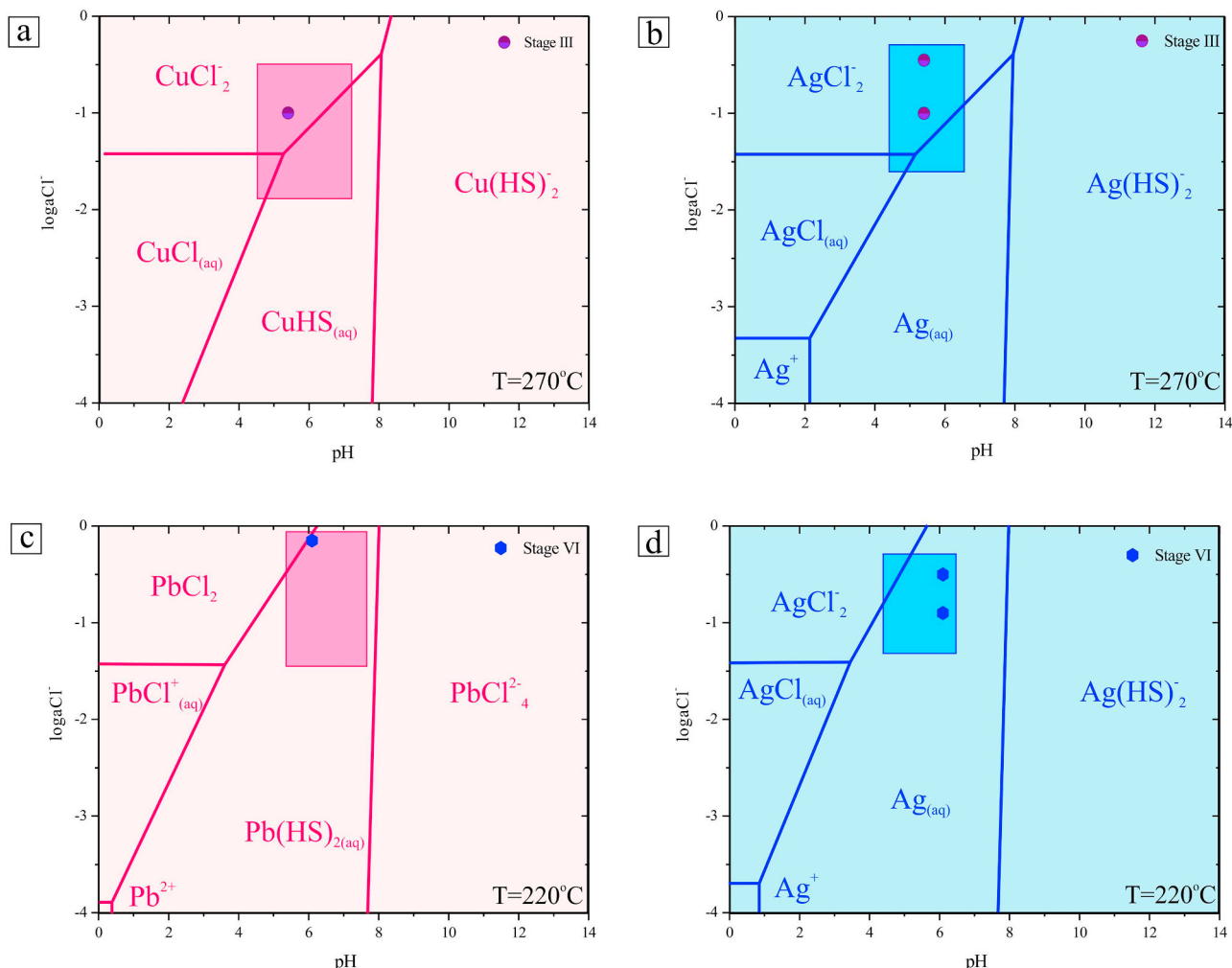**Fig. 5.** pH versus $\log aCl^-$ diagram for the Panormos Bay mineralizing fluid showing relationships: (a): at temperature of 270 °C, pressure of 500 bars and vapor saturation for the predominant Cu complexes related to precipitation of stage III chalcopyrite and bornite. Solution pH and activity of chloride were calculated using the properties of Plummer et al. (1988), and equations of state of Pitzer (1979, 1986), (b): at stage III, and for the same conditions for the predominant Ag complexes, (c): at temperature of 220 °C (stage VI), pressure of 500 bars and vapor saturation for the predominant Pb complexes, and (d): at stage VI, and for the same conditions for the predominant Ag complexes. The plots have drawn for an initial composition of the ore fluid of $\log a_{\Sigma Cl(aq)}^- = -1.1$, $\log a_{NaCl(aq)} = -1.4$ and $\log f_{\Sigma H2Te(g)} = -4$, and for $\log f_{O2} = -33$ and $\log a_{CuCl2(aq)}^- = -6.4$ (stage III), and $\log f_{O2} = -35$ and $\log PbCl_{2(aq)} = -4.5$ (stage VI). The shaded areas represent the stability field of the ore-forming conditions for T of 270° and 220 °C.

The next episodes of CO_2-effervescence and boiling which occurred at ~270 °C and ~220 °C associate to the precipitation of stage III chalcopyrite and bornite, and stage VI galena. Phase separation has affected likewise the He, Ar and Ne isotopic composition of these sulfides (Fig. 4a and b). Although there is overwhelming evidence for vapor transport of base and precious metals by the Panormos vapor-like ore fluid, it seems plausible that deposition of these metals occurred after condensation and contraction of the $H_2Te_{(g)}$-, $Te_{2(g)}$-, base- and precious-bearing laden vapors to Panormos ore liquid. Furthermore, Tombros et al. (2010) have suggested, due to the extreme enrichment of these sulfides in tellurium, that $H_2Te_{(g)}$ and $Te_{2(g)}$ is transported also to vapor (Cooke and McPhail, 2001) and then condensed, as droplets, in the Panormos ore liquid. Grundler et al. (2013) also reported, based on their experimental data and simulation, that calaverite and native Te coexist under reduced conditions and are in equilibrium with $Te_{2(g)}$ contained in the vapor phase.

Condensation of supersaturated vapors in the Panormos ore solution is evidenced by the observed textural relations (Fig. 2a to f), as well as, X-ray Ag and Au mapping (Fig. 2e and f), the occurrence of nanoparticles (Fig. 2d), and the chemical variance with various degree of enrichment for base and precious metal contents in stage II, III and VI

sulfides (Fig. 3a to h). Our thermodynamic calculations also support the concept that a fraction of the base and precious metals were primarily transported in the vapor phase than the liquid phase. Condensation of Panormos vapor phase allows the less dense, CO_2, $HCl_{(g)}$, $H_2S_{(g)}$, $H_2Te_{(g)}$, $Te_{2(g)}$, light noble gas isotopes, base- and precious-bearing laden vapors to cool and then contract (Simon et al., 2006) in the hybrid liquid. Also re-enriches the liquid ore phase in the light noble gas isotopes (e.g., ^3He, ^{36}Ar, ^{20}Ne and ^{21}Ne). So the $^3He/^4He$, $^{20}Ne/^{22}Ne$ and $^{21}Ne/^{22}Ne$ ratios tend to increase and the $^{40}Ar/^{36}Ar$ to decrease in the ore liquid (Fig. 4a). Moreover, condensation assisted $H_2Te_{(g)}$, $Te_{2(g)}$ and $H_2S_{(g)}$ to redistributed in the ore solution, gradually increase their concentrations and react with the base and precious metals complexes carried in solution to form the various sulfides of stages II, III and VI and stage V telluride mineral assemblages.

6. Conclusions

The Au-Ag-Te Panormos Bay mineralization is an illustrative example which verifies the importance of vapor transport for the base and precious metals, at epithermal conditions. The Panormos Bay aqueous mineralizing solution which is genetically related to Tinos leucogranite

(Tombros et al., 2007, 2010), initially transported dissolved $H_2Te_{(g)}$, and $Te_{2(g)}$ and base and precious metals into the epithermal environment. Therein it experienced CO_2-effervescence and boiling, leading a portion of CO_2, $HCl_{(g)}$, $H_2S_{(g)}$ and $H_2Te_{(g)}$, $Te_{2(g)}$ and light noble gas isotopes and base- and precious-bearing laden vapors to be preferentially partitioned and then transported into the gaseous phase. This vapor-like ore fluid achieved supersaturation, and then re-condensed into the epithermal ore liquid. This mechanism is essential for the formation of the Panormos Te-rich sulfide and telluride assemblages. Vapor transport and condensation contributed highly in their widespread precipitation, and the extensive variety of the observed tellurides at Panormos Au-Ag-Te ores.

Acknowledgements

References

Ahmad, M., Solomon, M., Walshe, J.L., 1987. Mineralogical and geochemical studies of the Emperor gold-telluride deposit, Fiji. Econ. Geol. 87, 345–370.

Alfieris, D., Voudouris, P., Spry, P.G., 2013. Shallow submarine epithermal Pb-Zn-Cu-Au-Ag-Te mineralization on western Milos Island, Aegean Volcanic Arc, Greece: mineralogical, geological and geochemical constraints. Ore Geol. Rev. 53, 159–180.

Andreassen, J.-P., Lewis, A.E., 2017. Classical and nonclassical theories of crystal growth. In: van Driessche, A., Kellermeier, M., Benning, L.G., Gebauer, D. (Eds.), New Perspectives on Mineral Nucleation and Growth From Solution Precursors to Solid Materials, pp. 137–154. https://doi.org/10.1007/978-3-319-45669-0_7.

Archibald, S.M., Migdisov, A.A., Williams-Jones, A.E., 2002. An experimental study of the stability of copper chloride complexes in water vapor at elevated temperatures and pressures. Geochim. Cosmochim. Acta 66, 1611–1619.

Bolhar, R., Ring, U., Allen, C.M., 2010. An integrated zircon geochronological and geochemical investigation into the Miocene plutonic evolution of the Cyclades, Aegean Sea, Greece: part 1: geochronology. Contr. Min. Petr. 160, 719–742.

Brichau, S., Ring, U., Carter, A., Monié, P., Bolhar, R., Stockli, D., Brunel, M., 2007. Extensional faulting on Tinos Island, Aegean Sea, Greece: how many detachments? Tectonics 26, TC4009. https://doi.org/10.1029/2006TC001969.

Brichau, S., Thomson, S., Ring, U., 2010. Thermochronometric constraints on the tectonic evolution of the Serifos detachment, Aegean Sea, Greece. Int. J. Earth Sci. (Geol. Rundsch) 99, 379–393. https://doi.org/10.1007/s00531-00008-00386-00530.

Bröcker, M., Franz, L., 1998. Rb-Sr isotope studies on Tinos Island (Cyclades, Greece): additional time constraints for metamorphism, extent of infiltration-controlled overprinting and deformational activity. Geol. Mag. 135, 369–382.

Bröcker, M., Franz, L., 2005. P-T conditions and timing of metamorphism at the base of the Cycladic blueschist Unit, Greece: the Panormos window on Tinos re-visited. N. Jah. Min. Abh. 181, 91–93.

Cooke, D.R., McPhail, D.C., 2001. Epithermal Au-Ag-Te mineralization, Acupan, Baguio district, Philippines: numerical simulations of mineral deposition. Econ. Geol. 96, 109–131.

Fulignati, P., Sbrana, A., 1998. Presence of native gold and tellurium in the active high-sulfidation hydrothermal system of the La Fossa volcano (Vulcano, Italy). J. Volcanol. Geotherm. Res. 86, 187–198.

Greenland, L.P., Aruscavage, P.J., 1986. Volcanic emissions of Se, Te, and As from Kilauea Volcano, Hawaii. J. Volcanol. Geotherm. Res. 27, 195–201.

Grundler, P.V., Brugger, J., Etschmann, B.E., Helm, L., Liu, W., Spry, P.G., Tian, Y., Testemale, D., Pring, A., 2013. Speciation of aqueous tellurium (IV) in hydrothermal solutions and vapors, and the role of oxidized tellurium species in Te transport and gold deposition. Geochim. Cosmochim. Acta 120, 298–325.

Heinrich, C.H., Ryan, C.G., Mernagh, T.P., Eadington, P.J., 1992. Segregation of ore metals between magmatic brine and vapor: a fluid inclusion study using PIXE microanalysis. Econ. Geol. 87, 1566–1583.

Henley, R.W., Truesdell, H.A., Whitney, J.A., Barton Jr., P.B., 1984. Fluid-mineral equilibria in hydrothermal systems. Rev. Econ. Geol. 1, 267.

Jolivet, L., Menant, A., Sternai, P., Rabillard, A., Arbaret, L., Augier, R., Laurent, V., Beaudoin, A., Grasemann, B., Huet, B., Labrousse, L., Le Pourhiet, L., 2015. The geological signature of a slab tear below the Aegean. Tectonophysics 659, 166–182. https://doi.org/10.1016/j.tecto.2015.08.004Get.

Katzir, Y., Avigad, D., Matthews, A., Garfunkel, Z., Evans, B.W., 2000. Origin, HP/LT metamorphism and cooling of ophiolitic mélanges in southern Evia (NW Cyclades), Greece. J. Metamorph. Geol. 18, 699–718.

Kendrick, M.A., Burnard, P., 2013. Noble gases and halogens in fluid inclusions: a journey through the Earth's crust. In: Burnard, P. (Ed.), The Noble Gases as Geochemical Tracers. Springer, Berlin Heidelberg, pp. 319–336.

Kendrick, M., Burgess, R., Pattrick, R.A.D., Turner, G., 2001. Halogen and Ar-Ar age determinations of fluid inclusions in quartz veins from porphyry copper deposits using complementary noble gas extraction techniques. Chem. Geol. 177, 351–370.

Knight, C.L., Bodnar, R.I., 1989. Synthetic fluid inclusions. IX. Critical PVTX properties of NaCl-H2O solutions. Geochim. Cosmochim. Acta 53, 3–8.

Larocque, A.C.L., Stimac, J.A., Siebe, C., Greengrass, K., Chapman, R., Melja, S.R., 2008. Deposition of high- sulfidation Au assemblage from a magmatic volatile phase, Volcan Popocatepetl, Mexico. J. Volcanol. Geotherm. Res. 170, 51–68.

Mastrakas, N., St. Seymour, K., 2000. Geochemistry of Tinos granite: a window to the Miocene microplate tectonics of the Aegean region. N. Jah. Min. Abh. 175, 295–315.

Mehl, C., Jolivet, L., Lacombe, O., Labrousse, L., Rimmele, G., 2007. Structural evolution of Andros (Cyclades, Greece): a key to the behaviour of a (flat) detachment within an extending continental crust. In: Taymaz, T., Yilmaz, Y., Dilek, Y. (Eds.), The Geodynamics of the Aegean and Anatolia. Geol. Soc. London, Spec. Publ, vol. 291. pp. 41–73.

Melidonis, N.G., 1980. The geological structure and mineral deposits of Tinos Island (Cyclades, Greece): a preliminary study. IGME 13, 80.

Migdisov, A.A., Williams-Jones, A.E., Suleimenov, O.M., 1999. The solubility of chlorargyrite (AgCl) in water vapor at elevated temperatures and pressures. Geochim. Cosmochim. Acta 63, 3817–3827.

Ohtaki, H., Radnai, T., 1993. Structure and dynamics of hydrated ions. Chem. Rev. 93, 1157–1204.

Okrusch, M., Bröcker, M., 1990. Eclogites associated with high-grade blueschists, Cyclades Archipelago, Greece. Eur. J. Mineral. 2, 451–478.

Pitzer, K.S., 1979. Theory: ion interaction approach. In: Pytkowicz, R.M. (Ed.), Activity Coefficients in Electrolyte Solutions. CRC Press, Inc., Boca Raton, Florida, pp. 157–208.

Pitzer, K.S., 1986. Theoretical considerations of solubility with emphasis on mixed aqueous electrolytes. Pure Appl. Chem. 58, 1599–1610.

Plummer, L.N., Parkhurst, D.L., Fleming, G.W., 1988. A computer program incorporating Pitzer's equations for calculating of geochemical reactions in rines. In: U.S. Geol. Survey Water-resources Investigations Report. Reston, Virginia, pp. 88–4153.

Pokrovski, G.S., Borisova, A.Y., Bychkov, A.Y., 2013. Speciation and transport of metals and metalloids in geological vapors. Rev. Mineral. Geochem. 76, 165–218.

Pudack, C., Halter, W.E., Heinrich, C.A., Pettke, T., 2009. Evolution of magmatic vapor to gold-rich epithermal liquid: the porphyry to epithermal transition at Nevados de Famatina, Northwest Argentina. Econ. Geol. 104, 449–477.

Rabillard, A., Arbaret, L., Jolivet, L., Le Breton, N., Gumiaux, C., Augier, R., Grasemann, B., 2015. Interactions between plutonism and detachments during metamorphic core complex formation, Serifos Island (Cyclades, Greece). Tectonics 34, 1080–1106. https://doi.org/10.1002/2014TC003650.

Rickard, D., Luther, G.W., 2006. III. Metal sulfide complexes and clusters. Rev. Mineral. Geochem. 61, 421–504.

Ronacher, E., Richards, J.P., Reed, M.H., Bray, C.J., Spooner, E.T.C., Adams, P.D., 2004. Characteristics and evolution of the hydrothermal fluid in the north zone high grade area, Porgera gold deposit, Papua New Guinea. Econ. Geol. 99, 843–867.

Saunders, J.A., 2012. Textural evidence of episodic introduction of metallic nanoparticles into Bonanza epithermal ores. Fortschr. Mineral. 2, 228–243. mdpi.com/2075-163X/2/3/228 (2014/11/29).

Seward, T.M., Driesner, T., 2004. Hydrothermal solution structure: experiments and computer simulations. In: Fernandez-Prini, R., Harvey, A.H., Palmer, D.A. (Eds.), Aqueous Systems at Elevated Temperatures and Pressures: Physical Chemistry in Water, Steam and Hydrothermal Solutions, pp. 149–182.

Seward, T.M., Williams, A.E., Migdisov, A.A., 2014. The chemistry of metal transport and deposition by ore-forming hydrothermal fluids. In: Holland, H., Turekian, K. (Eds.), Treatise on Geochemistry, 2nd edition. pp. 29–57.

Simon, A.C., Pettke, T., Candela, P.A., Piccoli, P.M., Heinrich, C.A., 2006. Copper partitioning in a melt-vapor-brine-magnetite-pyrrhotite assemblage. Geochim. Cosmochim. Acta 70, 5583–5600.

Spry, P.G., Paredes, M.M., Foster, F., Truckle, S.J., Chadwick, T.H., 1996. Evidence for a genetic link between gold-silver telluride and porphyry mineralization at the Golden Sunlight Deposit, Whitehall, Montana: fluid inclusion and stable isotopes studies. Econ. Geol. 91, 507–526.

St. Seymour, K., Mastrakas, N., Tombros, S.F., Williams-Jones, A.E., Spry, G., Denes, G., Kranidiotis, P., 2009. Scheelite mineralization of the skarn deposit, at Tinos Island, Aegean Sea, Cyclades. N. Jah. Min. Abh. 186, 37–50.

Stolz, J., Engi, M., Rickli, M., 1997. Tectonometamorphic evolution of SE Tinos, Cyclades, Greece. Schweiz. Mineral. Petrogr. Mitt. 77, 209–231.

Sugaki, A., Shima, H., Kitakaze, A., Harada, H., 1975. Isothermal phase relations in the system Cu-Fe-S under hydrothermal conditions at 350° and 300 °C. Econ. Geol. 70, 806–823.

Tempest, P.A., Ballentyne, D.W.G., 1974. Supersaturation control in crystal growth of II–VI compounds from the vapour. J. Cryst. Growth 21, 219–226.

Tombros, F.S., St. Seymour, K., Spry, P.G., 2004. Description and conditions of formation of new unnamed Ag-Cu and Ag-Cu-Au sulfotellurides in epithermal polymetallic Ag-Au-Te mineralization, Tinos Island, Hellas. N. Jah. Min. Abh. 179, 295–310.

Tombros, F.S., St. Seymour, K., Spry, P.G., Williams-Jones, A.E., 2005. Description and conditions of formation of new unnamed Zn-rich greenockite in epithermal polymetallic Ag-Au-Te mineralization, Tinos Island, Hellas. N. Jah. Min. Abh. Monastshefte 182, 1–9.

Tombros, F.S., St. Seymour, K., Williams-Jones, A.E., Spry, P.G., 2007. The genesis of epithermal Au-Ag-Te mineralization, Panormos Bay, Tinos Island, Cyclades, Hellas (Greece). Econ. Geol. 102, 1269–1294.

Tombros, F.S., St. Seymour, K., Williams-Jones, A.E., 2010. Explanation and conditions of formation of the high tellurium contents in the early and late base metals stages of the epithermal polymetallic Ag-Au-Te mineralization, Tinos Island, Hellas. Econ. Geol.

105, 1097–1111.

Trudu, A.G., Knittel, U., 1998. Crystallography, mineral chemistry and chemical nomenclature of goldfieldite, the tellurian member of the tetrahedrite solid-solution series. Can. Mineral. 36, 1115–1137.

Voudouris, P., Tarkian, M., Arikas, K., 2006. Mineralogy of telluride-bearing epithermal ores in Kassiteres-Sappes area, western Thrace, Greece. Mineral. Petrol. 87, 31–52.

Voudouris, P., Melfos, V., Spry, P.G., Moritz, R., Papavassiliou, K., Falalakis, G., 2011. Mineralogy and geochemical environment of formation of the Perama Hill high-sulfidation epithermal Au-Ag-Te-Se deposit, Petrota Graben, NE Greece. Mineral. Petrol. 103, 79–100.

Wallier, S., Rey, R., Kouzmanov, K., Pettke, T., Heinrich, C.A., Leary, S., O'Connor, G., Tamas, C.G., Vennemann, T., Ulrich, T., 2006. Magmatic fluids in the breccia-hosted epithermal Au-Ag deposit of Rosia Montana, Romania. Econ. Geol. 101, 923–954.

Wang, B.D., Niu, S.Y., Sun, A.Q., Hu, H.B., Liu, Y.M., Guo, L.J., Wang, S., 2008. Helium-argon-neon isotopic tracing for the Pb-Zn-Ag polymetallic ore deposits in the central-south segment of the Da Hinggan Ling Range. Chin. J. Geochem. 27235–27241.

Whitney, D., Evans, B., 2010. Abbreviations for names of rock-forming minerals. Am. Min. 95, 185–187.

Williams-Jones, A.E., Migdisov, A.A., 2014. Experimental constraints on the transport and deposition of metals in ore-forming hydrothermal systems. Econ. Geol. Spec. Pub. 18,

77–95.

Williams-Jones, A.E., Migdisov, A.A., Archibald, S.M., Xiao, Z., 2002. Vapor-transport of ore metals. In: David, A.C., Hellmann, R., Wood, S.A. (Eds.), Water-Rock Interactions, Ore Deposits, and Environmental Geochemistry. Geochem. Soc. Spec. Pub 7. pp. 279–306.

Xypolias, P., Iliopoulos, I., Chatzaras, V., Kokkalas, S., 2012. Subduction and exhumation related structures in the Cycladic Blueschists: insights from Evia Island (Aegean region, Greece). Tectonics 31, TC2001. https://doi.org/10.1029/2011TC002946.

Yudovskaya, M.A., Distler, V.V., Chaplygin, I.V., Mokhov, A.V., Trubkin, N.V., Gorbacheva, S.A., 2006. Gaseous transport and deposition of gold in magmatic fluid: evidence from the active Kudryavy volcano, Kurile Islands. Miner. Depos. 40, 828–848.

Zhai, D., Liu, J., Williams-Jones, A.E., Tombros, F.S., Cook, N.J., 2018. Mineralogical, fluid inclusion and multiple isotope (H-O-S-Pb) constraints on the genesis of the Sandaowanzi epithermal Au-Ag-Te deposit, NE China. Econ. Geol. 113, 1359–1382.

Zhu, M.-T., Zhang, L.-C., Wu, G., Cui, M.-L., 2013. Fluid inclusions and He-Ar isotopes in pyrite from the Yinjiagou deposit in the southern margin of the North China Craton: a mantle connection for poly-metallic mineralization. Chem. Geol. 351, 1–14. https://doi.org/10.1016/j.chemgeo.2013.05.004.